Metal-organic aerogels based on titanium(IV) for visible-light conducted CO_2 photoreduction to alcohols

Adrián Angulo-Ibáñez [a], Maite Perfecto-Irigaray [b], Ivan Merino-Garcia [c], Naia Luengo [b], Amaia M. Goitandia [a], Jonathan Albo [c, **], Estibaliz Aranzabe [a], Garikoitz Beobide [b, d, *], Oscar Castillo [b, d], Sonia Pérez-Yáñez [b, d]

[a] Surface Chemistry & Nanotechnologies Unit, Fdn Tekniker, Iñaki Goenaga 5, Eibar 20600, Spain
[b] Department of Organic and Inorganic Chemistry, University of the Basque Country, UPV/EHU, P.O. 644, E-48080 Bilbao, Spain
[c] Departamento de Ingenierías Química y Biomolecular, Universidad de Cantabria, Avda. Los Castros S/n, 39005 Santander, Spain
[d] BCMaterials, Basque Center for Materials, Applications and Nanostructures, UPV/EHU Science Park, 48940 Leioa, Spain

ARTICLE INFO

ABSTRACT

Metal-organic frameworks (MOFs) imply an appealing source of photocatalysts as they combine porosity with tailorable electronic properties and surface chemistry. Herein, we report a series of unprecedented metal-organic aerogels (MOAs) comprised by Ti(IV) oxo-clusters and aromatic dicarboxylic linkers as an alternative to microporous MIL-125 and MIL-125-NH_2 MOFs. Discrete titanium oxo-clusters polymerized upon the addition of the dicarboxylic linkers to give rise to a metal-organic gel. Their supercritical drying led to aerogels comprised by nanoscopic particles (ca. 5−10 nm) cross-linked into a meso/macroporous microstructure with surface area ranging from 453 to 617 $m^2 \cdot g^{-1}$, which are comparatively lower than the surface area of the microporous counterparts (1336 and 1145 $m^2 \cdot g^{-1}$, respectively). However, the meso/macroporous microstructure of MOAs can provide a more fluent diffusion of reagents and products than the intrinsic porosity of MOFs, whose narrower channels are expected to imply a more sluggish mass transport. In fact, the assessment of the continuous visible-light-driven photocatalytic CO_2 reduction into methanol shows that MOAs (221−786 $\mu mol \cdot g^{-1} \cdot h^{-1}$) far exceed not only the performance of their microporous counterparts (49−65 $\mu mol \cdot g^{-1} \cdot h^{-1}$) but also surpass the production rates provided by up-to-date reported photocatalysts.

© 2022 The Author(s). Published by Elsevier Ltd. This is an open access article under the CC BY-NC-ND license (http://creativecommons.org/licenses/by-nc-nd/4.0/).

1. Introduction

Global climate change has turned carbon dioxide (CO_2) emissions into a major environmental concern that demands cooperative international actions and implementation of technologies that can aid in reaching zero-net emissions [1]. In this context, CO_2 capture, storage, and revalorization technologies have been posited among the most promising solutions to mitigate the emission of greenhouse gases. Specifically, the transformation of CO_2 into value-added chemicals and fuels is envisaged as a promising chance to shift to a low-carbon economy and therefore contribute to substantially suppress the emissions of this greenhouse gas [2,3]. The transformation of CO_2 into products such as CO, CH_4, HCOOH,

HCHO, and CH_3OH can be carried out by thermochemical, electrochemical, biochemical, and photochemical methods [4,5]. Photochemical methods aim to mimic the natural photosynthesis systems by leading photo-driven CO_2 reduction or fixation reactions under mild conditions and without additional energy input, apart from solar irradiation [6,7]. The photochemical conversion of CO_2 into alcohols, such as methanol and ethanol, is of particular interest due to their great global demand as chemical feedstock and petroleum fuel substitute [8,9]. Accordingly, a great deal of attention has been devoted to the design of both the photoreactor and the photocatalyst [10]. Regarding the photocatalyst, wide band gap ultraviolet (UV) active semiconductors have been widely explored. Nonetheless, under natural sunlight illumination, visible/near infrared light active materials are expected to produce the maximum amount of charges to mediate the pursued reaction. Despite narrow band gap materials might present unsuitable potentials for simultaneously leading reduction and oxidation reactions, it can be overcome by using several strategies such as metal/non-metal doping, heterojunction formation, or

A. Angulo-Ibáñez, M. Perfecto-Irigaray, I. Merino-Garcia et al.

Materials Today Energy 30 (2022) 101178

photosensitizer anchoring [11]. High surface area is also a desirable feature for the photocatalyst as it can increase both the amount of adsorbed CO_2 and the amount of photogenerated electron/hole pairs with the potential to mediate the redox reactions. Considering the above facts, it becomes clear that nanostructured semi-conductors possess remarkable advantages over their bulk counterparts, such as their high surface-area-to-volume ratio, short charge migration distance, and tunable electronic properties [12]. In this regard, metal-organic frameworks (MOFs) present a nano-porous structure featured by great CO_2 adsorption capacity, extremely high surface-area-to-volume ratio, and a versatile electronic structure controlled by the assembly of the selected building blocks. Among them outstand those based on titanium(IV) and polycarboxylic ligands, such as the so-called materials institute lavoisier (MIL-125) and MIL-125-NH_2 MOFs, which have demonstrated to behave as promising photocatalysts in several reactions [13]. These MOFs are built by octanuclear titanium oxo-clusters 12-connected by ditopic organic linkers as depicted by the formula $[Ti_8(\mu\text{-}O)_8(\mu\text{-}OH)_4(\mu_4\text{-}L)_6]_n$, where L stands for benzene-1,4-dicarboxylato (BDC) or 2-aminobenzene-1,4-dicarboxylato (NH_2BDC) [14,15]. In terms of electronic structure, the metal clusters and organic ligands can be regarded as isolated semiconductor quantum dots and light-harvesting antennas, respectively, in such a way that the alignment of the bands that set the gap can be controlled through the molecular features of both, the ligand and the cluster and through their assembly [16−18]. According to density functional theory calculations, the highest occupied states are localized in the aromatic ligand and are mainly comprised by the π-electron cloud, whereas the lowest unoccupied states are localized in the octameric cluster, implying the empty 3d-orbitals of Ti(IV) [19,20]. The collation of the half-reaction potentials with the calculated valence band maximum and conduction band minimum allows inferring that these materials can a priori mediate the photocatalytic conversion of CO_2 (Fig. 1). In fact, CO_2 conversion

experiments using MIL-125 and MIL-125-NH_2 as photocatalysts have demonstrated the formation of HCOOH, CH_3OH, and CH_4 as reduction products [21,22].

Despite these materials have demonstrated their capability to photoreduce CO_2, their microporous structure suggests that the reaction rates could be markedly limited by the diffusion of the implied chemical species. Note that the 3D pore structure of these MOFs is comprised by cages of *ca.* 12 and 6 Å connected by windows of 5−7 Å, which are roughly greater than the kinetic diameters of CO_2 (3.30 Å) and some of its reduction products (CO: 3.76 Å; CH_3OH: 3.80 Å; C_2H_5OH: 4.6 Å) [24,25].

As diffusion coefficients markedly increase with the pore size and porosity [26,27], herein we report a series of unprecedented meso/macroporous metal-organic aerogels (MOAs) comprised by Ti(IV) oxo-clusters and dicarboxylic linkers (BDC and NH_2BDC) as an alternative to the microporous MIL-125 and MIL-125-NH_2 for the continuous photoreduction of CO_2 to alcohols (methanol and ethanol) under visible light. The results show that MOAs not only far exceed the performance of their microporous counterparts but also surpass the methanol production rates provided by up-to-date reported photocatalysts.

2. Materials and methods

2.1. Synthetic procedures

2.1.1. Reagents

All the chemicals (reagent grade) were used as commercially obtained. Titanium(IV) n-butoxide (TNBT, 98%) was purchased from Acros Organics (Geel, Belgium, EU). Titanium(IV) isoprop-oxide (99.8%), benzene-1,4-dicarboxylic acid (H_2BDC, 99%), 2-aminobenzene-1,4-dicarboxylic acid (H_2NH_2BDC, 99%), and N,N-dimethylformamide (DMF, 99%) were acquired from Sigma-Aldrich (Saint Louis, MO, USA). Absolute ethanol (EtOH), hydrochloric acid
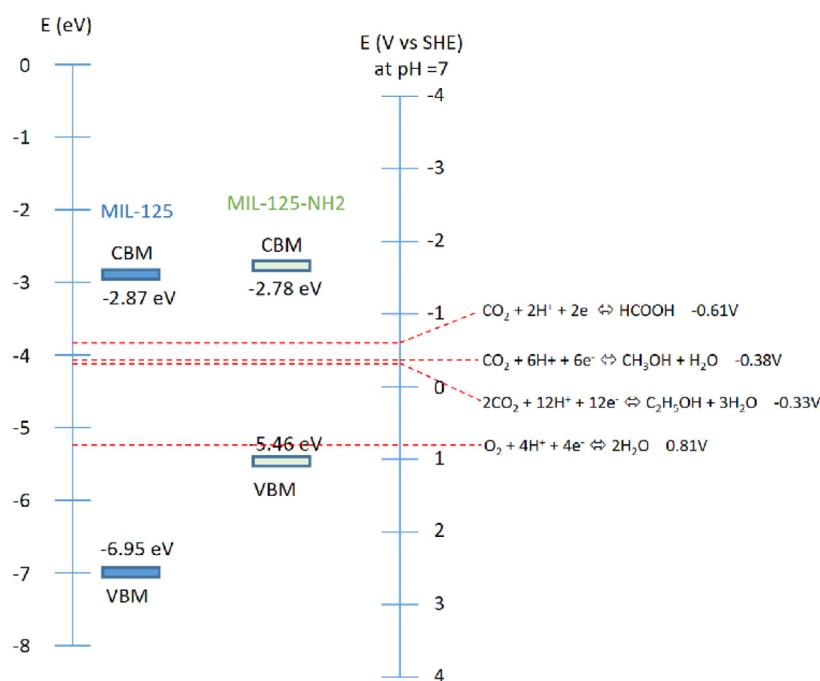

Fig. 1. Band alignment for MIL-125 and MIL-125-NH_2 compared to the potential of CO_2 reduction and water oxidation half-reactions at pH = 7. The values for VBM, CBM, and half-reaction potentials were retrieved from the literature [20,23]. In molecular materials, including MOFs, VBM, and CBM are also referred as frontier orbitals (HOMO: highest occupied molecular orbital; LUMO: lowest unoccupied molecular orbital). CBM, conduction band minimum; CO_2, carbon dioxide; MOF, metal-organic framework; VBM, valence band maximum.

A. Angulo-Ibáñez, M. Perfecto-Irigaray, I. Merino-Garcia et al.

Materials Today Energy 30 (2022) 101178

(HCl, 37%), and distilled water (H_2O) were provided by Scharlab, S.L. (Barcelona, Spain, EU).

2.1.2. Synthesis of MOAs

To prepare the metal-organic sols, first, titanium(IV) n-butoxide (3.17 mmol, 1.102 mL) was dissolved in 10 mL of 2-butanol. Thereafter, 4 mL of 2-butanol containing 118 μL of hydrochloric acid (0.29 M) were added dropwise over the first solution. This solution was stirred for 1 h in a sealed flask. Immediately after, a DMF/2-butanol (10 mL and 2 mL, respectively) solution of the source of the linkers (H_2BDC and/or H_2NH_2BDC) was added dropwise to the previous mixture. The total linker amount (2.38 mmol) was set to achieve a titanium:ligand molar ratio of 1:0.75, according to the ideal ratio found in MIL-125 and MIL-125-NH_2 titanium MOFs. The sample coding and the employed linker quantities are gathered in Table 1. The resulting clear solution evolved into a translucent metal-organic gel (MOG) after being aged for 6 h at 80 °C within a closed vessel. The obtained gels were stiff enough to retain the shape of the molds and/or were easily shapeable into regular geometries using cutting tools. The gels were subjected to successive solvent exchanges, first, with a mixture of 2-butanol/DMF (2:1) and a mixture of 2-butanol/DMF/ethanol (1:1:1) to remove the unreacted species and then with absolute ethanol to replace the remaining 2-butanol and DMF. The MOAs were prepared using an E3100 critical point dryer from Quorum Technologies equipped with a gas inlet, vent, and purge valves and with a thermal bath. First, the ethanol-exchanged gels were placed into the reactor chamber and then liquid CO_2 was introduced. The gels were maintained in liquid CO_2 at 293 K and 50 bar for 1 h. Afterward, the exchanged ethanol was released through the purge valve. The liquid CO_2 exchange process was repeated five times to ensure the removal of ethanol. Subsequently, the temperature and the pressure of the chamber were increased to 313 K and 85−95 bar in order to set supercritical conditions. Finally, under constant temperature (313 K), the chamber was slowly vented up to atmospheric pressure. The obtained aerogels retained the shape of the parent gels. Note that drying the gels via conventional solvent evaporation induced a severe contraction of the microstructure and led to non-porous xerogels.

2.1.3. Synthesis of MIL-125 and MIL-125-NH_2

MIL-125 and MIL-125-NH_2 were prepared by following previously reported procedures [15,28]. Specifically, to synthesize MIL-125, 9 mmol of titanium isopropoxide and 15 mmol of benzene-1,4-dicarboxylic acid were dissolved in a 50 mL mixture of DMF and methanol (9:1, v/v) under stirring. The resulting mixture was introduced into a Teflon-lined autoclave reactor and heated at 423 K in an oven during 16 h. After cooling down, a white polycrystalline powder was filtered off and thoroughly washed, first, with DMF and then with methanol. The compound was dried in an oven to remove the solvent molecules. MIL-125-NH_2 was synthesized following the same procedure but using 3 mmol of titanium isopropoxide and 6 mmol of 2-amino-1,4-benzene dicarboxylic

acid. The obtained yellowish polycrystalline powder was again filtered off, washed with DMF and methanol, and dried in an oven.

2.2. Characterization

2.2.1. Chemical characterization

Powder X-ray diffraction (PXRD) patterns were measured at 20 °C on a Phillips X'PERT diffractometer (Cu-Kα radiation, λ = 1.5418 Å) in the 5−50° 2θ range and using a step size of 0.02°, a variable automatic divergence slit, and an acquisition time of 2.5 s per step. Fourier transform infrared (FTIR) spectra of the samples dispersed in KBr pellets were recorded in the 4000−400 cm^{-1} range with a resolution of 4 cm^{-1} using a FTIR 8400S Shimadzu spectrometer. Thermogravimetric analysis curves were measured from room temperature to 800 °C on a METTLER TOLEDO thermogravimetric analysis/SDTA851 thermal analyzer using a flux of 50 cm^3 min^{-1} of synthetic air (80% N_2, 20% O_2), a heating rate of 5 °C min^{-1}, and 10−20 mg of sample per run. Proton nuclear magnetic resonance (^{1}H-NMR) spectra were recorded at 293 K using a Bruker AVANCE 500 (one-bay; 500 MHz). Prior to ^{1}H-NMR measurements, a sample (50 mg) of the corresponding compound was digested in 2 mL of a 1 M NaOH solution (in deuterated water, D_2O) during 1 h in an opaque flask. Thereafter, fumaric acid (14 mg) was added as an internal standard. The remaining solid residue corresponding to titanium(IV) oxide was filtered off and the NMR spectrum was taken on the liquid fraction. X-ray photoelectron spectroscopy measurements were performed in a SPECS system (Berlin, Germany) equipped with a Phoibos 150 1D-DLD analyzer and Al Kα monochromatic radiation source (1486.7 eV). An initial analysis was carried out to determine the elements present (wide scan: step energy 1 eV, dwell time 0.1 s, pass energy 80 eV) and detailed analysis of the detected elements was performed (detail scan: step energy 0.08 eV, dwell time 0.1 s, pass energy 30 eV) with an electron exit angle of 90°. The spectrometer was previously calibrated with Ag (Ag $3d_{5/2}$, 368.26 eV). Spectra were fitted using CasaXPS 2.3.16 software, which models Gauss-Lorentzian contributions, after background subtraction (Shirley).

2.2.2. Electrospray ionization mass spectrometry

The electrospray ionization mass spectrometry (ESI-MS) spectra were measured by injecting the reaction mixture at a flow rate of 20 μL·min^{-1} into a high resolution mass spectrometer (Synapt G2, time of flight analyzer) equipped with an ESI source in positive and negative mode. The high resolution spectra were recorded in scan mode, with a mass range of 30−2500 Da in resolution mode (FWHM ≈ 20,000) and a scan time of 0.1 s. The source and desolvation temperatures were 120 and 350 °C, respectively. The capillary voltage was set to 2.5 kV (negative), while the cone voltage was maintained at 15 V. N_2 was used as the desolvation and cone gas, with the flow rates of 600 and 10 L·h^{-1}. Prior to analysis, the mass spectrometer was calibrated using a sodium formate solution and a leucine-enkephalin solution for the lock mass correction, monitoring the ions at mass-to-charge ratio (*m/z*) 556.2771. All of the acquired spectra were automatically corrected during acquisition based on the lock mass.

2.2.3. Electron microscopy

The microstructure of the samples was analyzed by transmission electron microscopy (TEM), in a TECNAI G2 20 TWIN (FEI company), operating at an accelerating voltage of 200 KeV in a bright-field image mode and a low-dose image mode. The samples for room temperature TEM were prepared dispersing an aerogel sample onto a TEM copper grid (300 Mesh) covered by a holey carbon film. For cryogenic TEM measurements, the solvent of a gel sample was exchanged with water. Then, a 3 μL aliquot of sample

Table 1
Sample coding and the corresponding amounts of bridging ligands.[a]

Sample	H_2BDC		H_2NH_2BDC	
	mmol	g	mmol	g
B100A0	2.38	0.403	0	0.000
B75A25	1.78	0.302	0.6	0.110
B50A50	1.19	0.202	1.19	0.218
B25A75	0.6	0.102	1.78	0.326
B0A100	0	0.000	2.38	0.435

[a] In the sample coding, B and A stand for BDC and NH_2BDC, respectively, while the targeted ligand ratio is represented by numeric characters.

A. Angulo-Ibáñez, M. Perfecto-Irigaray, I. Merino-Garcia et al.

Materials Today Energy 30 (2022) 101178

suspension was applied to glow-discharged 300 mesh lacey carbon TEM grids and used for plunge freezing into liquid ethane on a Vitrobot Mark IV (FEI company). The frozen grids were then transferred to a 626 DH Single Tilt Cryo-Holder (Gatan, France), maintained below −170 °C (liquid nitrogen temperature), and then, they were transferred to TEM chamber at liquid nitrogen temperature. Field emission scanning electron microscopy images were recorded on a Hitachi S-4800 using aerogel samples previously metallized with a gold layer of 15 nm.

2.2.4. Dinitrogen and CO₂ adsorption measurements

N_2 (77 K) and CO_2 (273 and 298 K) adsorption data were acquired using a Quantachrome Autosorb-iQ MP gas sorption analyzer. The samples were outgassed under vacuum at 140 °C for 6 h, prior to measurements. The values of the specific surface area were calculated by the fitting of the N_2 adsorption curve to Brunauer−Emmett−Teller (BET) equation [29]. In order to choose the pressure range for the fitting and to avoid ambiguity when reporting the BET surface area of materials containing micropores, we used the three consistency criteria proposed by Rouquerol et al. [30]: (1) The pressure range selected should have values of V(1-P/P_0) increasing with P/P_0. (2) The points used to calculate the BET surface area must be linear with an upward slope in such a way that the linear regression must yield a positive y-intercept (i.e., positive C value). (3) The P/P_0 value corresponding to V_m should be within the BET fitting range. The CO_2 adsorption enthalpies (Q_{st}) were estimated by fitting the adsorption isotherms to the modified Clausius−Clapeyron equation [31,32]. The micropore volume of the samples was estimated according to the t-plot method [33].

2.2.5. Diffuse reflectance spectra

Diffuse reflectance spectra of the samples were measured on an UV/VIS/near-infrared PerkinElmer Lambda 950 spectrophotometer equipped with an integrating sphere (150 mm Int. Sphere). The spectra were measured over the range 250−800 nm with a resolution of 1 nm.

2.2.6. Photoreduction of CO₂ in an optofluidic microreactor

Prior to their use, all metal-organic materials were outgassed at 150 °C under vacuum. The light-responsive surfaces were prepared by depositing the MOA onto porous carbon papers (Toray TGP-H-60), following a previously reported procedure [34]. The airbrushing process is carried out at 100 °C to ensure the complete evaporation of the solvent (isopropanol) during the accumulation of photocatalytic layers. The total MOA mass loading per photoelectrode was set to 2 mg·cm⁻², which is experimentally determined by continuous weighing. The porous carbon paper containing the metal-organic material was assembled in a home-made designed planar optofluidic microreactor (APRIA Systems S.L.), equipped with a reaction microchamber of 1 cm² and 75 μL, for the continuous light-driven transformation of CO_2 into alcohols (see further details in the Supplementary Data). The photoactive surfaces were placed in the reaction microchamber and irradiated with light-emitting diode (LED) lights (peak at 450 nm) with a light intensity of E = 5 mW·cm⁻² measured by a radiometer (Photo-radiometer Delta OHM) and controlled by adjusting the LED intensity and the distance between the microreactor and the LED. A full description of the experimental setup and photoreactor details can be found elsewhere [34].

A CO_2 saturated 0.5 M KHCO₃ (Panreac >97%) aqueous solution (pH = 7.38 ± 0.03) was prepared with ultra-pure water (18.2 MΩ cm at 273 K, MilliQ Millipore system) and supplied to the reactor microchamber with a micropump (Minipuls 3 Gilson) at a flow rate of Q_L = 100 μL·min⁻¹. The photochemical CO_2 reduction tests were carried out by duplicate in continuous mode for 120 min, when a

pseudo-stable performance is reached. The optofluidic microreactor was placed in a ventilated dark box and the temperature was controlled with an infrared thermometer (ca. 20 °C). The concentration of alcohols in each sample was analyzed by duplicate in a headspace gas chromatograph (GCMS-QP2010 Ultra Shimadzu) equipped with a flame ionization detector. An average concentration was obtained for each point (error less than 12.3%). The performance of the process is analyzed in terms of reaction rates (r), i.e. product yield per gram of photocatalyst and time. The apparent quantum yield (AQY) is defined as $(n_e/n_p) \cdot 100$, where n_e represents the rate of electrons transferred toward CH_3OH and C_2H_5OH, defined as the number of molecules evolved (mol) multiplied by the number of reacted electrons (6 and 12 e⁻ for CH_3OH and C_2H_5OH, respectively) and the Avogadro's number (mol⁻¹). On the contrary, n_p is the rate of incident photons on the surface, calculated according to equation (1):

$$n_p = \frac{E \cdot A \cdot t \cdot \lambda}{h \cdot C} \qquad \text{Equation 1}$$

where E is the light intensity (W·m⁻²), A represents the irradiation area (m²), t is the reaction time (s), λ corresponds to the wavelength peak (m), h is the Planck's constant (J·s), and C represents the speed of light (m·s⁻¹), respectively.

3. Results and discussion

3.1. Chemical and microstructural characterization

Solution chemistry of Ti(IV) implies the formation of titanium oxo-clusters of different nuclearity depending on the used solvent, water amount, pH, and ligands [35]. In this sense, ESI-MS measurements have allowed us to analyze the speciation of the titanium complexes in the reaction mixture. Prior to the addition of the bridging ligand, collected mass spectra reveal the formation of a series of octanuclear Ti_8O_8 cores in which the remaining coordination positions and charge balance are provided by water/butanol molecules and hydroxide/butoxide anions (Fig. 2). The different peaks appearing in the spectra are not compatible with other cluster nuclearities and their differences come from the exchange among the ligands/anions that complete the outer coordination sphere. To provide further evidence, a comparison of the maximum intensity peak (($m/z)_{max}$) and the width of the isotopic peak distribution ($\Delta_{m/z}$) values subtracted from the experimental and simulated ESI(+)-MS spectra has been included in Table S1. It deserves to note that the intensity of the experimental peaks is determined by the concentration of each species in the solution. On the other hand, the addition of the bridging carboxylic ligand to the reaction mixture does not meaningfully change the speciation in solution according to the collected ESI(+)-MS spectra (Fig. S1). This fact suggests that the polymerization reaction takes place upon heating the reactor, implying the replacement of the coordinated molecules of the pre-assembled octameric entities by the dicarboxylic ligands. Note that this type of octanuclear Ti_8O_8 clusters are also commonly found in carboxylate-based MOFs and discrete complexes [36].

During the synthesis, the metal clusters are cross-linked by means of benzene-1,4-dicarboxylato (BDC) and/or aminobenzene-1,4-dicarboxylato (NH₂BDC) ligands to yield a polymeric MOG. The synthesis solvent and unreacted reagents trapped within the MOG were replaced by ethanol. Then, each MOG was supercritically dried to yield the corresponding MOA (Fig. 3). Despite a slight contraction takes place during the aerogel formation, the monoliths still retain a remarkable porosity as below described.

According to the chemical analysis, the BDC/NH₂BDC linker ratio was close to that employed in the synthesis (Table S2). Nonetheless,
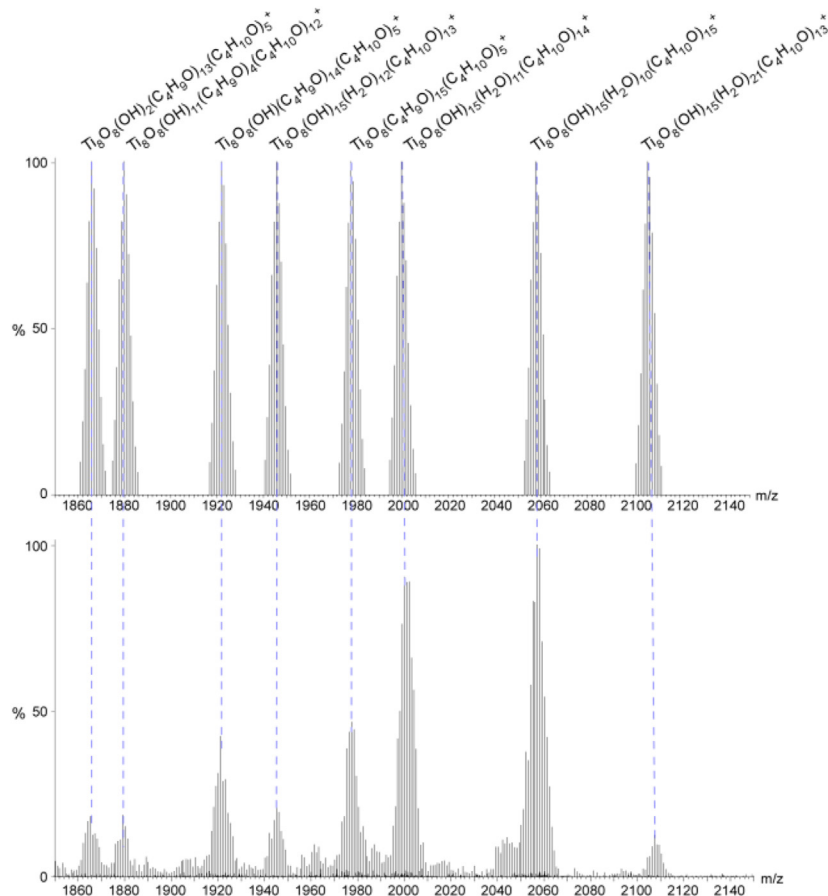
Fig. 2. Comparison of the experimental ESI(+)-MS spectrum of the reagent mixture (down) with the one simulated (up) from the molecular formulas of the octameric species. Computed peaks cannot deal with the concentration of the species, and thus, the resulting spectrum represents an equimolar speciation that does not aim to match the observed intensity values. ESI-MS, electrospray ionization mass spectrometry.

in comparison with the referential MIL-125 and MIL-125-NH$_2$, the formulas present a meaningful amount of linker vacancies (58−60%) that are replaced by H$_2$O/OH$^-$ pairs and formate anions to balance the charge and the coordination positions, as it also
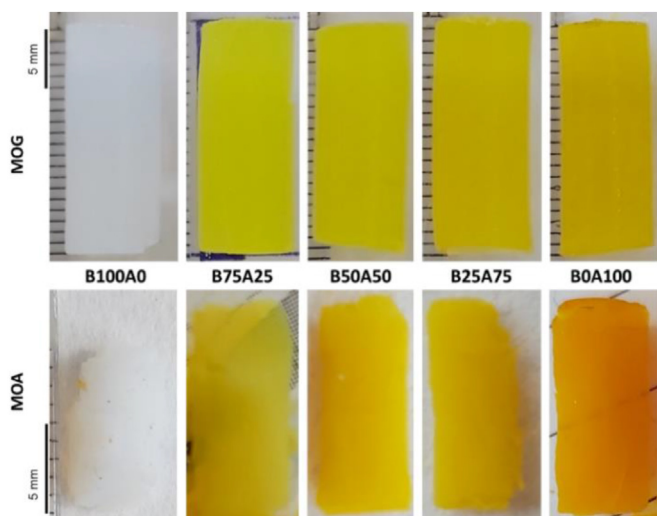
Fig. 3. Synthesized MOGs and MOAs with varying BDC/NH$_2$BDC ratio. BDC, benzene-1,4-dicarboxylato; MOA, metal-organic aerogel; MOG, metal-organic gel.
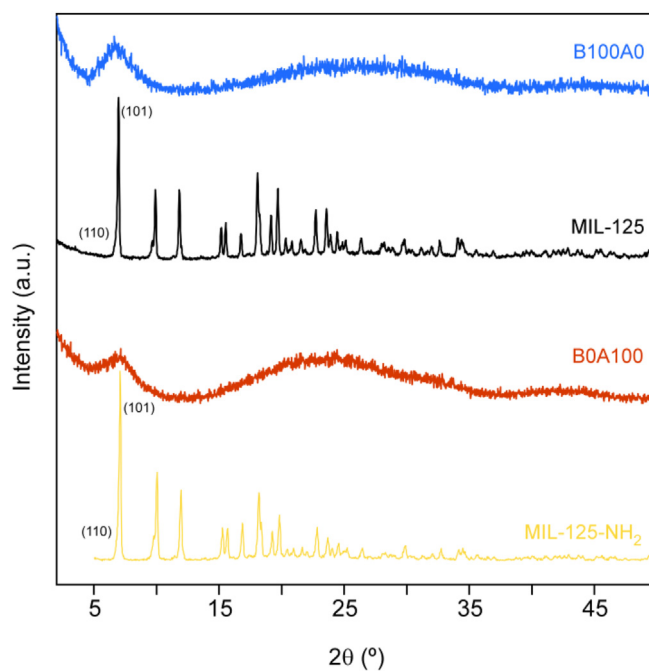

Fig. 4. PXRD patterns of referential MOFs (MIL-125 and MIL-125-NH$_2$) compared to B100A0 and B0A100 MOAs. MOA, metal-organic aerogel; MOF, metal-organic framework; PXRD, powder X-ray diffraction.
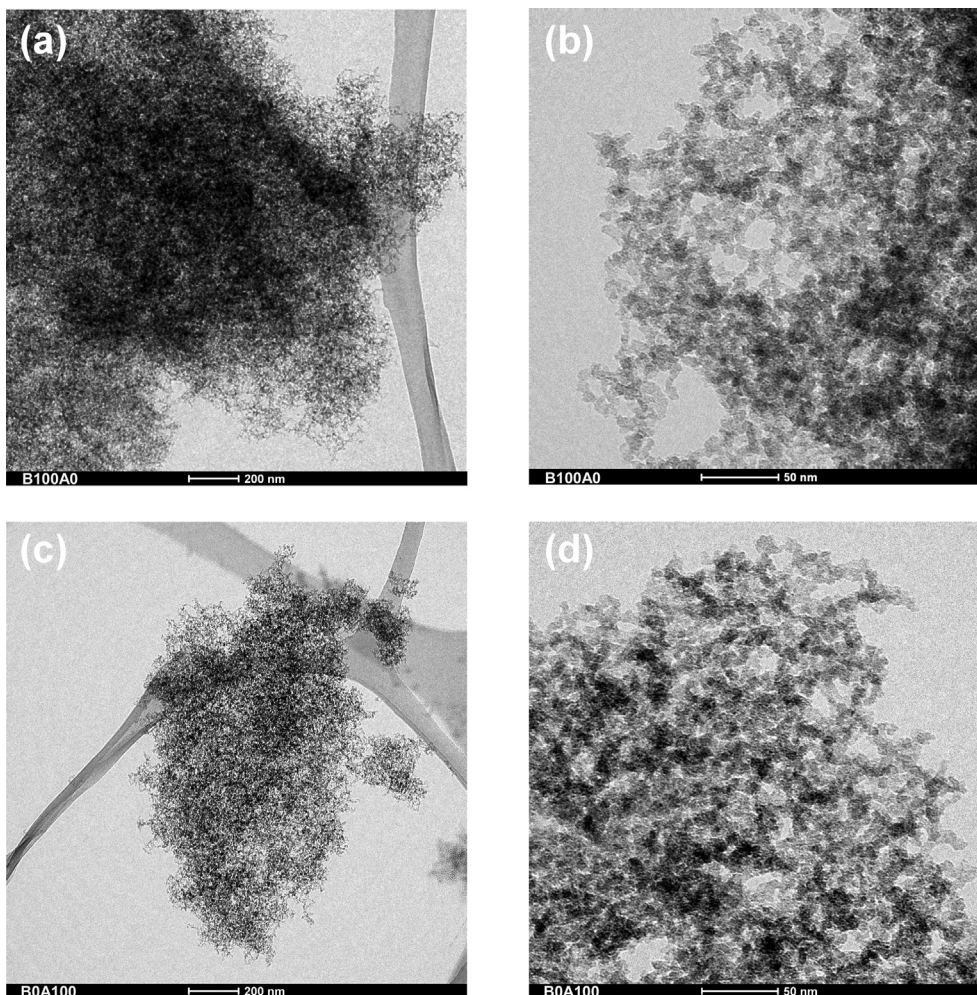
Fig. 5. TEM images on aerogel fragments of B100A0 at (**a**) 25 kX and (**b**) 150 kX magnifications and B0A100 at (c) 25 kX and (d) 150 kX magnifications. TEM, transmission electron microscopy.

occurs in the defective MOFs of group IV metals [37,38]. As a result, each cluster seems to be connected through *ca.* 5 linkers per cluster. Interestingly, the PXRD patterns of the herein prepared MOAs show a broad maximum at $2\theta = 6.4-6.7°$. This maximum agrees fairly well with the maximum intensity peak of MIL-125 and MIL-125-NH_2 ($2\theta = 6.8°$), which arises from the combined contribution of (101) and (110) reflections and is related to the interplanar distance set by the BDC/NH_2BDC linkers between titanium cluster arrays ($d_{101} = 13.0$ Å; $d_{101} = 13.2$ Å) (Fig. 4). The whole-pattern fitting of the PXRD data of the crystalline MOFs is included in the supplementary data (Fig. S10 and Tables S3 and S4).

Furthermore, the X-ray photoemission measurements (Fig. S3 of the supplementary data) show the distinctive 2p peaks of titanium(IV) ($2p_{3/2}$ and $2p_{1/2}$: 459 and 465 eV, respectively) whose position fit well to the data available in the literature for MOFs with Ti_8O_8 type clusters showing hexacoordinated TiO_6 environments ($2p_{3/2}$ and $2p_{1/2}$: 458−459 and 464−465 eV) [39,40]. The molecular structure of the materials was further supported by FTIR spectroscopy. The collected spectra and assignation of the main vibration modes are shown in Fig. S2. The inclusion of the NH_2BDC ligand is evidenced by the bands found at 3460 and 3350 cm^{-1} related to the N−H stretching of the amino group. The C−H stretching of the linkers
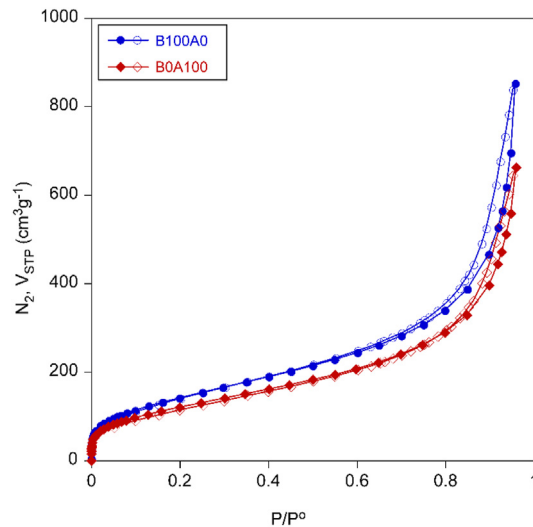

Fig. 6. N_2 physisorption isotherms at 77 K for B100A0 and B0A100 MOAs. Filled and empty symbols imply adsorption and desorption data, respectively.

Table 2
Porosity data for titanium(IV)-based MOAs and referential microporous MOFs.[a]

Sample	S_{BET} ($m^2 \cdot g^{-1}$)	S_{micro} ($m^2 \cdot g^{-1}$)	S_{ext} ($m^2 \cdot g^{-1}$)	V_{micro} ($cm^3 \cdot g^{-1}$)	V_{ext} ($cm^3 \cdot g^{-1}$)
B100A0	531	38	493	0.013	1.318
B75A25	504	31	473	0.008	1.201
B50A50	617	70	547	0.027	1.242
B25A75	539	52	487	0.018	1.504
B0A100	453	33	420	0.010	1.026
MIL-125	1336	1258	78	0.493	0.579
NH$_2$-MIL-125	1145	1089	56	0.422	0.486

[a] S_{BET} stands for BET specific surface area. Micropore surface area (S_{micro}) and volume (V_{micro}) are estimated from the t-plot calculation. External surface area (S_{ext}) is calculated by subtracting the microporous contribution from the total area. V_T is the total pore volume for pores $\leq$50 nm.

(BDC and NH$_2$BDC) are observable at 3200−2800 cm^{-1} range. The anti-symmetric stretching of the carboxylate groups of the formate anion and organic linkers (BDC and NH$_2$BDC) are observed at 1645 cm^{-1} and 1540−1570 cm^{-1}, respectively.

TEM images collected on MOA samples show a microstructure comprised of partially sintered metal-organic tiny nanoparticles of 5−10 nm (Fig. 5). According to the micrographs, the stochastic entanglement of these particles during gelling process generates a nanoporous network comprised by voids of random shape and size. The relative BDC/NH$_2$BDC ratio of the compound did not exert any meaningful differences in the microstructure. Further electron microscopy images can be found in the supplementary data (Fig. S12).

Besides, cryogenic TEM images taken on MOG samples (Fig. S11) show similar microstructural features to that described for MOAs, which supports the suitability of the followed supercritical drying process. Note that the analysis of the gel upon cryogenic conditions (see Experimental Section) allows for observing its pristine structure, as it avoids the microstructural changes (including pore collapse or particle sintering) that would take place upon gel drying in ambient temperature measurement.

3.2. Gas physisorption measurements

The porosity of the aerogels was further analyzed by measuring N$_2$ adsorption isotherms at 77 K (Fig. 6 and Fig. S15). Table 2 summarizes the resulting porosity data. For comparative purposes, we have also included the gas sorption data of the herein prepared referential microporous MIL-125 and MIL-125-NH$_2$ MOFs. The gas sorption curves of all MOAs resemble a type II/IV isotherm according to the IUPAC classification [41], with a steep hysteresis loop at high relative pressures (P/P > 0.8), which indicates that porosity is mainly determined by the joint contribution of meso- and macropores, accordingly to the expectations of TEM analysis. Fitting of the adsorption data to the BET equation yielded specific surface areas ranging from 453 to 617 m$^2 \cdot$g^{-1}, while total pore volumes varied between 1.03 and 1.50 cm$^3 \cdot$g^{-1}.

According to the data subtracted from the t-plot analysis, the microporosity implies only a minor contribution to the total surface area and pore volume of the MOAs, which can be ascribed to the scarce crystallinity of the coordination network. As expected, the two referential MOFs show a type I isotherms (Fig. S15) with surface area values far greater than those of MOAs and close to those previously reported.

On the other hand, CO$_2$ adsorption isotherms were measured at 273 and 298 K to calculate the isosteric heats of adsorption (Q$_{st}$) (Fig. S16 and Fig. S17). The Q$_{st}$ values at near-zero coverage range from 24 to 30 kJ·mol^{-1}. These values are comparable to those reported for other MOFs [42]. Thereafter, they decay progressively to values of 14−20 kJ·mol^{-1} when the gas loading gets a ratio of ca. 0.4 CO$_2$ mmol·g^{-1}. The inclusion of NH$_2$BDC ligand leads to
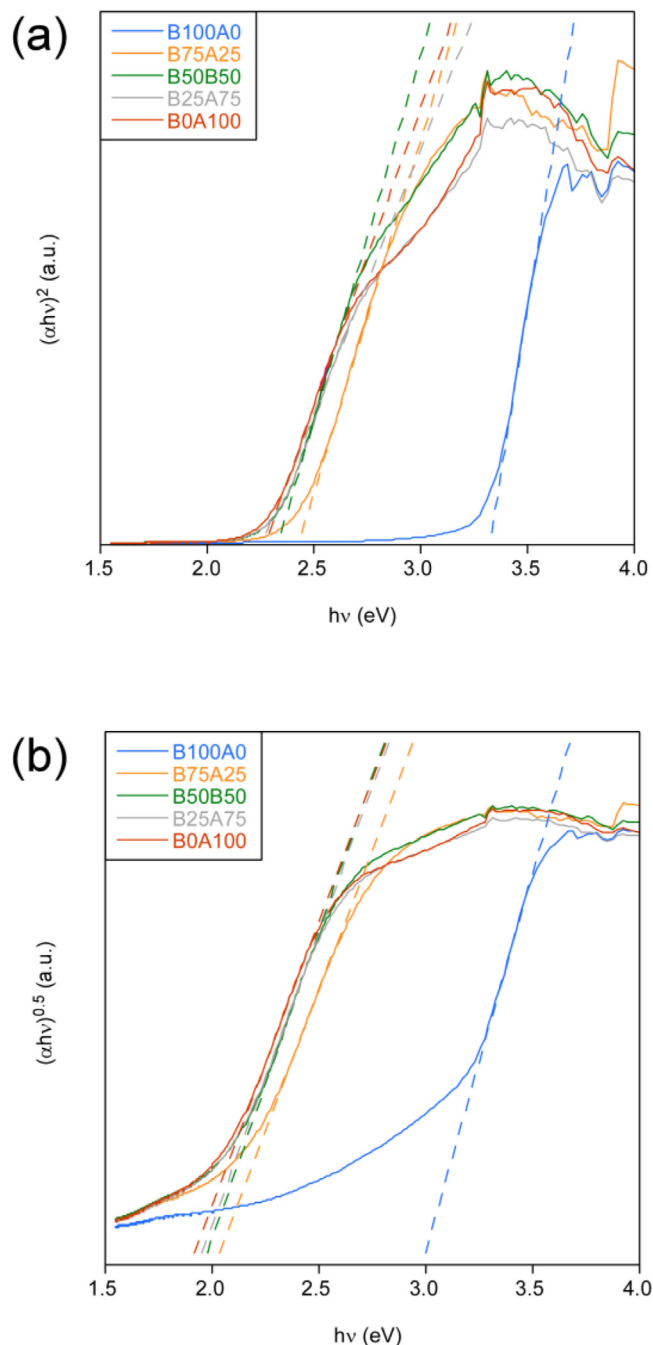

Fig. 7. (αhν)$^{1/n}$ vs. hν plots for each MOA, depicting the linear fit to Tauc equation (dashed lines) for (**a**) direct and (**b**) indirect band gaps. MOA, metal-organic aerogel.

A. Angulo-Ibáñez, M. Perfecto-Irigaray, I. Merino-Garcia et al.

Materials Today Energy 30 (2022) 101178

Table 3
Optical direct and indirect band gap values calculated from the Tauc method.

Sample	E_g (eV)	
	direct	indirect
B100A0	3.32	2.98
B75A25	2.43	2.01
B50A50	2.33	1.96
B25A75	2.26	1.93
B0A100	2.27	1.90

somewhat greater isosteric heat values (*ca.* +5 kJ·mol^{-1}) in samples B50A50, B25A75, and B0A100, which can be attributed to a favored interaction between the amino group and CO_2 molecule. Such trend has also been reported for other amino-functionalized porous compounds [43].·

3.3. Optical band gap

To calculate the optical band gap (E_g) values, the UV-visible diffuse reflectance spectra of the MOAs were transformed to the corresponding absorption spectra by applying the Kubelka−Munk function [44]. The resulting data were fitted to Tauc's formula, $(\alpha h\nu)^{1/n} = A(h\nu - E_g)$, where, α is the absorption coefficient, A is a constant, hν is photon energy, and n is a factor that depends on the band gap electron transition: 0.5 for direct and 2 for indirect transitions [45,46]. The band gap value is obtained from the intersection of the linear fit with the abscissa axis in the $(\alpha h\nu)^{1/n}$ vs. hν plot (Fig. 7). The optical band gap values calculated for direct and indirect transition are shown in Table 3. Accordingly, the increase of the NH_2BDC/BDC ratio promote a progressive narrowing of the band gap values with the increase of relative NH_2BDC content, reaching a minimum for B25A75 and B0A100. Such redshift can be ascribed to the energy rise of the π-bonding molecular orbitals comprising the highest occupied molecular orbital of the complex entity taking place upon the inclusion of the amino functional group [21]. The band gap values determined for B100A0 and B0A100 are comparable to their microporous MOF counterparts MIL-125 and MIL-125-NH_2 (range of optical E_g values calculated for direct transitions: 3.8−3.2 eV and 2.8−2.4, respectively) [20,47,48].

3.4. Photocatalytic conversion of CO_2

The performance of the MOAs as photocatalysts for CO_2 photoreduction was tested in a micro-optofluidic reactor equipped with a visible light LED. In all cases, the analysis of the liquid fraction revealed the formation of meaningful amounts of both methanol and ethanol, with also trace amounts of formic acid, which is likely intermediate specie in the CO_2 conversion to methanol [49]. Despite gas-phase products were not analyzed, previous tests on the use of TiO_2-based coated carbon papers in the same optofluidic microreactor and operating conditions under visible light irradiation [34,50] showed that only small quantities

of CO and CH_4 can be detected (AQY <0.05%). Note that CO_2-reduction liquid-phase products were not detected in the blank tests conducted in the absence of illumination or without CO_2. The achieved reaction rates (r) and AQY for each product are presented in Table 4. All MOAs exhibit superior formation rates of methanol (range: 221−786 μmol·g^{-1}·h^{-1}) with respect to ethanol (201−218 μmol·g^{-1}·h^{-1}). The upper limit for the reaction rates of both methanol and ethanol formation is achieved for B50A50. Contrarily, the lowest performance is provided by B0A100, which might not only be related to its comparatively lower external surface area (Table 2), but it could also be associated with the energy increase of highest occupied molecular orbital level of the complex entity containing NH_2BDC ligands, which would render a lower potential to conduct complementary water oxidation reaction (Fig. 1). The stability of the photocatalytic materials was tested for 6 h of continuous operation under visible light (5 mW·cm^{-2}). The methanol and ethanol production rates were roughly stable during all the assessed time. Fig. 8 displays, as an example, the evolution of the production rate of alcohols with time for the MOA B50A50.

To assess the relevance of the external surface area provided by the MOAs, we have prepared and analyzed the photocatalytic performance of the analogous microporous MIL-125 and MIL-125-NH_2 MOFs under the same reaction conditions (Table 4). The values obtained are similar to those reported by other authors in the CO_2 to methanol conversion using this type of MOFs [21]. Although these referential MOFs have much greater surface area values (Table 2), their performance in the optofluidic microreactor is comparatively low. Such difference can in part be ascribed to the sluggish diffusion of reagent molecules, intermediates, and products along the narrow-sized micropores. Conversely, the meso/macropores of MOAs endow an agile transit of the chemical species during their conversion into reduced products. In any case, defect chemistry of MOAs, featured by a meaningful amount of OH^-/H_2O pairs replacing linker vacancies, can also play an important role in the overall performance. In this regard, the lowest unoccupied molecular orbital of this kind of metal-organic polymers is comprised by the empty d-orbitals of the titanium, so the linker vacancies of MOAs might pave the transfer of the photoelectron since the approach of CO_2 would be sterically less hindered than in the linker-saturated titanium cluster (secondary building unit) comprising the ideal MOFs.

For comparative purposes, we have retrieved the CO_2-to-methanol photocatalytic formation rates provided so far by best performing inorganic materials, MOFs and MOF composites (Fig. 9, Tables S6 and S7). Due to the data abundance for inorganic materials, the studies providing methanol production rates below 100 μmol·g^{-1}·h^{-1} have not been considered. It results clear that all MOAs, except, B0A100 exceed by far the rates provided by MOFs. The greatest reported performances for photocatalysts based on metal-organic materials correspond to a MOF nanocomposite of MIL-125 with CuO and graphitic carbon nitride (342 μmol·g^{-1}·h^{-1}) [51] and to a neat MOF termed as ZIF-8(Cu) (332 μmol·g^{-1}·h^{-1}),

Table 4
Methanol and ethanol production rates and apparent quantum yields under visible light illumination (5 mW/cm^2) at 2 h of reaction.

Aerogel	r_{CH_3OH} (μmol·g^{-1}·h^{-1})	$r_{C_2H_5OH}$ (μmol·g^{-1}·h^{-1})	AQY_{CH_3OH} (%)	$AQY_{C_2H_5OH}$ (%)
B100A0	674.2	145.2	12.0	5.2
B75A25	650.8	128.3	11.5	4.6
B50A50	786.5	218.2	14.0	7.7
B25A75	716.3	101.6	12.7	3.6
B0A100	221.0	200.6	3.9	7.1
MIL-125	48.8	0	0.9	0
MIL-125-NH_2	64.6	0	0	0

A. Angulo-Ibáñez, M. Perfecto-Irigaray, I. Merino-Garcia et al.

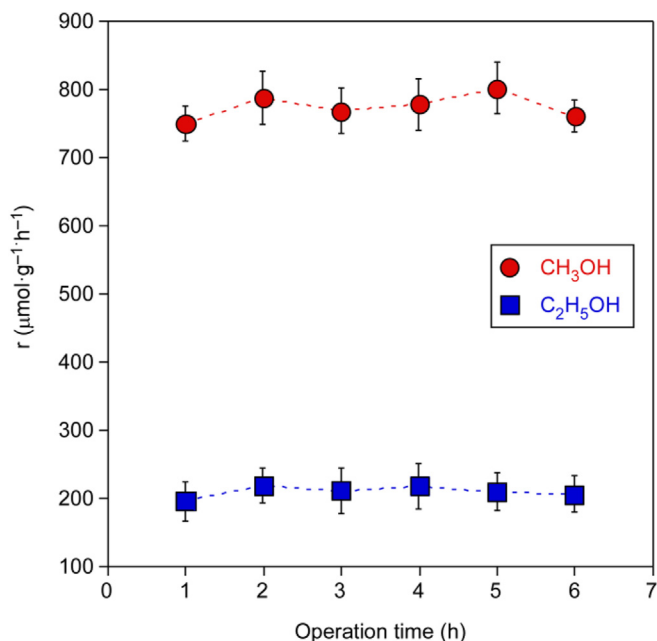Materials Today Energy 30 (2022) 101178

Fig. 8. Continuous visible light-driven CO_2 photoreduction to alcohols with B50A50.

respectively [52]. Nonetheless, the maximum rate reached for the latter neat MOF required the use of a sacrificial reagent as hole scavenger (sodium sulphite), which is an inconvenient with regard to the system using solely water. The remaining reported metal-organic materials render more modest production rate values that range within $7-63\ \mu mol \cdot g^{-1} \cdot h^{-1}$. The analyzed data also show that all Ti/BDC MOAs, except B0A100, overpass the best performing
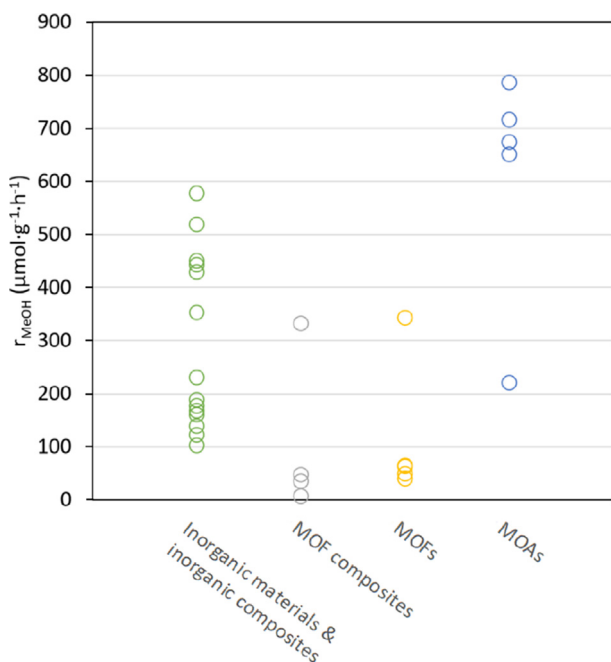
Fig. 9. MeOH formation rates in the photocatalytic reduction of CO_2 provided by best-performing state-of-the-art catalysts (inorganic materials, MOF composites and neat MOFs) compared to the herein reported Ti/BDC MOAs. For the inorganic catalysts results with rates below $100\ \mu mol \cdot g^{-1} \cdot h^{-1}$ are not presented. BDC, benzene-1,4-dicarboxylato; MOA, metal-organic aerogel.

state-of-the-art inorganic photocatalysts. In this case, the highest reaction rates (519 and 577 $\mu mol \cdot g^{-1} \cdot h^{-1}$) were achieved using TiO_2 nanoparticles (ca. 11 nm) doped with copper and carbon as photocatalyst [53,54].

4. Conclusions

This work covers the synthesis, characterization, and utilization of a series of unprecedented MOAs comprised by Ti(IV) oxo-clusters and aromatic dicarboxylic linkers for visible light-driven CO_2 photoreduction to alcohols. ESI-MS analysis of the reaction media revealed the presence of discrete octanuclear titanium oxo-clusters which polymerize upon the addition of a rigid dicarboxylic linker (BDC or NH_2BDC) to give rise to MOGs. The supercritical drying of the gels led to aerogels (MOAs) comprised by nanoscopic particles (ca. 5–10 nm) cross-linked into a meso/macroporous microstructure with surface area values ranging from 453 to 617 $m^2 \cdot g^{-1}$, which are comparatively lower than the surface area values of the referential microporous MIL-125 and MIL-125-NH_2 MOFs (1336 and 1145 $m^2 \cdot g^{-1}$, respectively).

These types of MOAs and MOFs can be regarded as an appealing alternative to conventional photocatalysts, as both combine porosity with tailorable electronic properties and surface chemistry based on the selection of the molecular building blocks that comprise the coordination polymer. However, MOAs are featured by a meso/macroporous microstructure that can provide an improved diffusion of the reagents and products than the intrinsic porosity of MOFs whose narrower channels are expected to imply a more sluggish mass transport. Such feature seems to play a key role providing a superior performance for MOAs in the photocatalytic conversion of CO_2 that beats by far the performance of MOFs. Besides, the herein reported titanium(IV) MOAs also overpass the photochemical CO_2-to-methanol reaction rates provided by the state-of-the-art inorganic materials and composites. All in all, MOAs built from the assembly of titanium oxo-cluster and benzene-1,4-dicarboxylato ligand represent a promising type of visible-light active photocatalyst that can imply a meaningful advance in the CO_2 conversion technologies. Nonetheless, further work is desirable in order to enlighten the underlying reaction mechanism, assess the performance under natural sunlight and find synergistic blends, or doping strategies that can boost further the reaction rates in order to approach the performance of mature electrochemical technologies, without additional energy input apart from the solar irradiation.

Credit authorship contribution statement

G. B., J. A. and E. A. conceived the experiments and wrote manuscript. A. A.-I., M. P.-I, I. M.-G and N. L. conducted the synthesis, characterizations and photocatalytic experiments; O. C., A. M. G. and S. P.-Y. analyzed the results. All authors reviewed the manuscript.

Declaration of competing interest

Data availability

Data will be made available on request.

Acknowledgments

Appendix A. Supplementary data

Supplementary data to this article can be found online at https://doi.org/10.1016/j.mtener.2022.101178.

References

[1] 2021 United Nations Climate Change Conference, COP26, Glasgow, (n.d.). https://www.ukcop26.org (accessed 24 March 2022).

[2] S. Perathoner, G. Centi, CO₂ recycling: a key strategy to introduce green energy in the chemical production chain, ChemSusChem 7 (2014) 1274−1282, https://doi.org/10.1002/cssc.201300926.

[3] Z. Zhang, S.Y. Pan, H. Li, J. Cai, A.G. Olabi, E.J. Anthony, V. Manovic, Recent advances in carbon dioxide utilization, Renew. Sustain. Energy Rev. 125 (2020), 109799, https://doi.org/10.1016/j.rser.2020.109799.

[4] F.O. Ochedi, D. Liu, J. Yu, A. Hussain, Y. Liu, Photocatalytic, electrocatalytic and photoelectrocatalytic conversion of carbon dioxide: a review, Environ. Chem. Lett. 19 (2021) 941−967, https://doi.org/10.1007/s10311-020-01131-5.

[5] O.S. Bushuyev, P. De Luna, C.T. Dinh, L. Tao, G. Saur, J. van de Lagemaat, S.O. Kelley, E.H. Sargent, What should we make with CO₂ and how can we make it? Joule 2 (2018) 825−832, https://doi.org/10.1016/j.joule.2017.09.003.

[6] P.R. Yaashikaa, P. Senthil Kumar, S.J. Varjani, A. Saravanan, A review on photochemical, biochemical and electrochemical transformation of CO₂ into value-added products, J. CO2 Util. 33 (2019) 131−147, https://doi.org/10.1016/j.jcou.2019.05.017.

[7] W. Tu, Y. Zhou, Z. Zou, Photocatalytic conversion of CO₂ into renewable hydrocarbon fuels: state-of-the-art accomplishment, challenges, and prospects, Adv. Mater. 26 (2014) 4607−4626, https://doi.org/10.1002/adma.201400087.

[8] J. Wu, Y. Huang, W. Ye, Y. Li, CO₂ reduction: from the electrochemical to photochemical approach, Adv. Sci. 4 (2017), 1700194, https://doi.org/10.1002/advs.201700194.

[9] L.M. de Lima, M.R.P. Bacchi, Chapter 13 - global ethanol market: commercialization trends, regulations, and key drivers, in: A.K. Chandel, M.H.L. Silveira (Eds.), Advances in Sugarcane Biorefinery, Elsevier, 2018, pp. 253−277, https://doi.org/10.1016/B978-0-12-804534-3.00013-6.

[10] E. Gong, S. Ali, C.B. Hiragond, H.S. Kim, N.S. Powar, D. Kim, H. Kim, S.-I. In, Solar fuels: research and development strategies to accelerate photocatalytic CO₂ conversion into hydrocarbon fuels, Energy Environ. Sci. 15 (2022) 880−937, https://doi.org/10.1039/d1ee02714j.

[11] X. Li, J. Yu, M. Jaroniec, X. Chen, Cocatalysts for selective photoreduction of CO₂ into solar fuels, Chem. Rev. 119 (2019) 3962−4179, https://doi.org/10.1021/acs.chemrev.8b00400.

[12] X. Chen, C. Li, M. Grätzel, R. Kostecki, S.S. Mao, Nanomaterials for renewable energy production and storage, Chem. Soc. Rev. 41 (2012) 7909−7937, https://doi.org/10.1039/c2cs35230c.

[13] R. Li, W. Zhang, K. Zhou, Metal−organic-framework-based catalysts for photoreduction of CO₂, Adv. Mater. 30 (2018), 1705512, https://doi.org/10.1002/adma.201705512.

[14] M. Dan-Hardi, C. Serre, T. Frot, L. Rozes, G. Maurin, C. Sanchez, G. Férey, A new photoactive crystalline highly porous titanium(IV) dicarboxylate, J. Am. Chem. Soc. 131 (2009) 10857−10859, https://doi.org/10.1021/ja903726m.

[15] C. Zlotea, D. Phanon, M. Mazaj, D. Heurtaux, V. Guillerm, C. Serre, P. Horcajada, T. Devic, E. Magnier, F. Cuevas, G. Férey, P.L. Llewellyn, M. Latroche, Effect of NH₂ and CF₃ functionalization on the hydrogen sorption properties of MOFs, J. Chem. Soc., Dalton Trans. 40 (2011) 4879−4881, https://doi.org/10.1039/c1dt10115c.

[16] M.A. Nasalevich, M. Van Der Veen, F. Kapteijn, J. Gascon, Metal-organic frameworks as heterogeneous photocatalysts: advantages and challenges, CrystEngComm 16 (2014) 4919−4926, https://doi.org/10.1039/c4ce00032c.

[17] S. Bordiga, C. Lamberti, G. Ricchiardi, L. Regli, F. Bonino, A. Damin, K.-P. Lillerud, M. Bjorgen, A. Zecchina, Electronic and vibrational properties of a MOF-5 metal-organic framework: ZnO quantum dot behaviour, Chem. Commun. (2004) 2300−2301, https://doi.org/10.1039/b407246d.

[18] N. Kolobov, M.G. Goesten, J. Gascon, Metal−organic frameworks: molecules or semiconductors in photocatalysis? Angew. Chem., Int. Ed. 60 (2021) 26038−26052, https://doi.org/10.1002/anie.202103642.

[19] A. Walsh, C.R.A. Catlow, Photostimulated reduction processes in a titania hybrid metal-organic framework, ChemPhysChem 11 (2010) 2341−2344, https://doi.org/10.1002/cphc.201000306.

[20] Y. Li, Y. Fu, B. Ni, K. Ding, W. Chen, K. Wu, X. Huang, Y. Zhang, Effects of ligand functionalization on the photocatalytic properties of titanium-based MOF: a density functional theory study, AIP Adv. 8 (2018), 035012, https://doi.org/10.1063/1.5021098.

[21] J.O. Olowoyo, U. Saini, M. Kumar, H. Valdés, H. Singh, M.O. Omorogie, J.O. Babalola, A.V. Vorontsov, U. Kumar, P.G. Smirniotis, Reduced graphene oxide/NH₂-MIL-125(Ti) composite: selective CO₂ photoreduction to methanol under visible light and computational insights into charge separation, J. CO2 Util. 42 (2020), 101300, https://doi.org/10.1016/j.jcou.2020.101300.

[22] Y. Fu, D. Sun, Y. Chen, R. Huang, Z. Ding, X. Fu, Z. Li, An amine-functionalized titanium metal-organic framework photocatalyst with visible-light-induced activity for CO₂ reduction, Angew. Chem., Int. Ed. 51 (2012) 3364−3367, https://doi.org/10.1002/anie.201108357.

[23] A. Sartorel, M. Bonchio, S. Campagna, F. Scandola, Tetrametallic molecular catalysts for photochemical water oxidation, Chem. Soc. Rev. 42 (2013) 2262−2280, https://doi.org/10.1039/c2cs35287g.

[24] R.W. Baker, Membrane transport theory, in: Membr. Technol. Appl., John Wiley & Sons, 2012, pp. 15−96, https://doi.org/10.1002/9781118359686.ch2.

[25] T.C. Bowen, S. Li, R.D. Noble, J.L. Falconer, Driving force for pervaporation through zeolite membranes, J. Membr. Sci. 225 (2003) 165−176, https://doi.org/10.1016/j.memsci.2003.07.016.

[26] D. Mu, Z.S. Liu, C. Huang, N. Djilali, Determination of the effective diffusion coefficient in porous media including Knudsen effects, Microfluid, Nanofluid 4 (2008) 257−260, https://doi.org/10.1007/s10404-007-0182-3.

[27] H. Long, H.-f. Lin, M. Yan, Y. Bai, X. Tong, X.-g. Kong, S.-g. Li, Adsorption and diffusion characteristics of CH₄, CO₂, and N₂ in micropores and mesopores of bituminous coal: molecular dynamics, Fuel 292 (2021), 120268, https://doi.org/10.1016/j.fuel.2021.120268.

[28] S.-N. Kim, J. Kim, H.-Y. Kim, H.-Y. Cho, W.-S. Ahn, Adsorption/catalytic properties of MIL-125 and NH₂-MIL-125, Catal, Today Off. 204 (2013) 85−93, https://doi.org/10.1016/j.cattod.2012.08.014.

[29] S. Brunauer, P.H. Emmett, E. Teller, Adsorption of gases in multimolecular layers, J. Am. Chem. Soc. 60 (1938) 309−319, https://doi.org/10.1021/ja01269a023.

[30] J. Rouquerol, P. Llewellyn, F. Rouquerol, Is the BET equation applicable to microporous adsorbents? Stud. Surf. Sci. Catal. 160 (2007) 49−56, https://doi.org/10.1016/s0167-2991(07)80008-5.

[31] K. Sumida, D.L. Rogow, J.A. Mason, T.M. McDonald, E.D. Bloch, Z.R. Herm, T.-H. Bae, J.R. Long, Carbon dioxide capture in metal-organic frameworks, Chem. Rev. 112 (2012) 724−781, https://doi.org/10.1021/cr2003272.

[32] H. Pan, J.A. Ritter, P.B. Balbuena, Isosteric heats of adsorption on carbon predicted by density functional theory, Ind. Eng. Chem. Res. 37 (1998) 1159−1166, https://doi.org/10.1021/ie9705867.

[33] B.C. Lippens, J.H. de Boer, Studies on pore systems in catalysts: V. The t method, J. Catal. 4 (1965) 319−323, https://doi.org/10.1016/0021-9517(65)90307-6.

[34] J. Albo, M.I. Qadir, M. Samperi, J.A. Fernandes, I. de Pedro, J. Dupont, Use of an optofluidic microreactor and Cu nanoparticles synthesized in ionic liquid and embedded in TiO₂ for an efficient photoreduction of CO₂ to methanol, Chem. Eng. J. 404 (2021), 126643, https://doi.org/10.1016/j.cej.2020.126643.

[35] H. Assi, G. Mouchaham, N. Steunou, T. Devic, C. Serre, Titanium coordination compounds: from discrete metal complexes to metal-organic frameworks, Chem. Soc. Rev. 46 (2017) 3431−3452, https://doi.org/10.1039/c7cs00001d.

[36] S. Wang, H. Reinsch, N. Heymans, M. Wahiduzzaman, C. Martineau-Corcos, G. De Weireld, G. Maurin, C. Serre, Toward a rational design of titanium metal-organic frameworks, Matter 2 (2020) 440−450, https://doi.org/10.1016/j.matt.2019.11.002.

[37] S. Yuan, J.-S. Qin, C.T. Lollar, H.C. Zhou, Stable metal-organic frameworks with group 4 metals: current status and trends, ACS Cent. Sci. 4 (2018) 440−450, https://doi.org/10.1021/acscentsci.8b00073.

[38] M. Perfecto-Irigaray, J. Casanova-Chafer, G. Beobide, S. Calero, O. Castillo, I. Da Silva, J.J. Gutierrez Sevillano, A. Luque, S. Pérez-Yáñez, L.F. Velasco, Metastable Zr/Hf-MOFs: the hexagonal family of EHU-30 and their water-sorption induced structural transformation, Inorg. Chem. Front. 8 (2021) 4767−4779, https://doi.org/10.1039/d1qi00997d.

[39] Y. Fu, H. Yang, R. Du, G. Tu, C. Xu, F. Zhang, M. Fan, W. Zhu, Enhanced photocatalytic CO₂ reduction over Co-doped NH₂-MIL-125(Ti) under visible light, RSC Adv. 7 (2017) 42819−42825, https://doi.org/10.1039/c7ra06324e.

[40] H. Xiao, W. Zhang, Q. Yao, L. Huang, L. Chen, B. Boury, Z. Chen, Zn-free MOFs like MIL-53(Al) and MIL-125(Ti) for the preparation of defect-rich, ultrafine ZnO nanosheets with high photocatalytic performance, Appl. Catal. B Environ. 244 (2019) 719−731, https://doi.org/10.1016/j.apcatb.2018.11.026.

[41] M. Thommes, K. Kaneko, A.V. Neimark, J.P. Olivier, F. Rodriguez-Reinoso, J. Rouquerol, K.S.W. Sing, Physisorption of gases, with special reference to the evaluation of surface area and pore size distribution (IUPAC Technical Report), Pure Appl. Chem. 87 (2015) 1051−1069, https://doi.org/10.1515/pac-2014-1117.

[42] J.-R. Li, Y. Ma, M.C. McCarthy, J. Sculley, J. Yu, H.-K. Jeong, P.B. Balbuena, H.-C. Zhou, Carbon dioxide capture-related gas adsorption and separation in metal-organic frameworks, Coord. Chem. Rev. 255 (2011) 1791−1823, https://doi.org/10.1016/j.ccr.2011.02.012.

[43] Z. Zhang, Z.-Z. Yao, S. Xiang, B. Chen, Perspective of microporous metal-organic frameworks for CO_2 capture and separation, Energy Environ. Sci. 7 (2014) 2868−2899, https://doi.org/10.1039/c4ee00143e.

[44] P. Kubelka, F. Munk, A contribution to the optics of pigments, Z. Technol. Phys. 12 (1931) 593−599.

[45] J. Tauc, R. Grigorovici, A. Vancu, Optical properties and electronic structure of amorphous germanium, Phys. Status Solidi B 15 (1966) 627−637, https://doi.org/10.1002/pssb.19660150224.

[46] P. Makuła, M. Pacia, W. Macyk, How to correctly determine the band gap energy of modified memiconductor photocatalysts based on UV-Vis spectra, J. Phys. Chem. Lett. 9 (2018) 6814−6817, https://doi.org/10.1021/acs.jpclett.8b02892.

[47] J. Wang, A.S. Cherevan, C. Hannecart, S. Naghdi, S.P. Nandan, T. Gupta, D. Eder, Ti-based MOFs: new insights on the impact of ligand composition and hole scavengers on stability, charge separation and photocatalytic hydrogen evolution, Appl. Catal. B Environ. 283 (2021), 119626, https://doi.org/10.1016/j.apcatb.2020.119626.

[48] N.J. Castellanos, Z. Martinez Rojas, H.A. Camargo, S. Biswas, G. Granados-Oliveros, Congo red decomposition by photocatalytic formation of hydroxyl radicals (·OH) using titanium metal−organic frameworks, Transit. Met. Chem. 44 (2019) 77−87, https://doi.org/10.1007/s11243-018-0271-z.

[49] L. Liu, Y. Li, Understanding the reaction mechanism of photocatalytic reduction of CO_2 with H_2O on TiO_2-based photocatalysts: a Review, Aerosol Air Qual. Res. 14 (2014) 453−469, https://doi.org/10.4209/aaqr.2013.06.0186.

[50] J. Albo, G. García, Enhanced visible-light photoreduction of CO_2 to methanol over Mo_2C/TiO_2 surfaces in an optofluidic microreactor, React. Chem. Eng. 6 (2021) 304−312, https://doi.org/10.1039/D0RE00376J.

[51] N. Li, X. Liu, J. Zhou, W. Chen, M. Liu, Encapsulating CuO quantum dots in MIL-125(Ti) coupled with g-C_3N_4 for efficient photocatalytic CO_2 reduction, Chem. Eng. J. 399 (2020), 125782, https://doi.org/10.1016/j.cej.2020.125782.

[52] J. Li, D. Luo, C. Yang, S. He, S. Chen, J. Lin, L. Zhu, X. Li, Copper(II) imidazolate frameworks as highly efficient photocatalysts for reduction of CO_2 into methanol under visible light irradiation, J. Solid State Chem. 203 (2013) 154−159, https://doi.org/10.1016/j.jssc.2013.04.016.

[53] Y.N. Kavil, Y.A. Shaban, R.K. Al Farawati, M.I. Orif, M. Zobidi, S.U.M. Khan, Photocatalytic conversion of CO_2 into methanol over Cu-C/TiO_2 nanoparticles under UV light and natural sunlight, J. Photochem. Photobiol. A-Chem. 347 (2017) 244−253, https://doi.org/10.1016/j.jphotochem.2017.07.046.

[54] Y.N. Kavil, Y.A. Shaban, R.K. Al Farawati, M.I. Orif, M. Zobidi, S.U.M. Khan, Efficient photocatalytic reduction of CO_2 present in seawater into methanol over Cu/C-Co-doped TiO_2 nanocatalyst under UV and natural sunlight, Water Air Soil Pollut. 229 (2018) 1−14, https://doi.org/10.1007/s11270-018-3881-3.